

IMAGE-DOMAIN MATERIAL DECOMPOSITION USING DATA-DRIVEN SPARSITY MODELS FOR DUAL-ENERGY CT

Zhipeng Li[†], Saiprasad Ravishankar*, Yong Long[†], Jeffrey A. Fessler*

[†] University of Michigan - Shanghai Jiao Tong University Joint Institute,
 Shanghai Jiao Tong University, Shanghai, China

*Department of Electrical Engineering and Computer Science, University of Michigan, MI, USA

ABSTRACT

Penalized weighted least squares (PWLS) with better image priors is a promising way to develop improved image-domain dual-energy CT (DECT) methods for achieving high quality basis material images. We propose a new method for DECT that combines conventional PWLS estimation with regularization based on sparsifying transforms (DECT-ST) learned from datasets of numerous CT images. Numerical experiments with phantom and patient data show that the proposed method significantly improves the image quality over direct matrix inversion decomposition and over PWLS decomposition with an edge-preserving hyperbola regularizer (DECT-EP).

Index Terms— Dual-energy CT, Sparsifying transform learning, Basis material decomposition, Machine learning.

1. INTRODUCTION

Dual-energy CT (DECT) enables characterizing concentration of constituent materials (e.g., soft tissue and bone) in scanned objects, known as material decomposition [1]. The decomposed material images are useful for many clinical and industrial applications, such as kidney stone characterization and liver-fat quantification. Image-domain decomposition methods [2, 3] for DECT decompose reconstructed CT images at high and low energies into material images. Image-domain methods are more practical than projection-domain [4] and direct decomposition methods [5] that both require sinograms or pre-log measurements that are not directly available on commercial DECT scanners. However, image-domain methods are susceptible to artifacts (e.g., beam-hardening artifacts) and noise in reconstructed CT images, especially for low dose imaging.

Existing big databases of CT images could be exploited to learn or adapt priors for improving image-domain DECT methods. Xu et al. [6] applied dictionary learning to CT image reconstruction by proposing a PWLS approach with

regularization based on a trained redundant dictionary. Then dictionary learning methods were applied to DECT for denoising [7] and reconstruction [8, 9]. A generalized analysis dictionary learning method called sparsifying transform (ST) learning [10] provides promising performance in low-dose CT image reconstruction [11]. In contrast to the often highly non-convex and NP-hard dictionary learning problems, the transform model can be learned efficiently [10] due to the simple thresholding-based sparse coding in the transform domain. This paper proposes a new image-domain dual-material decomposition method for DECT that combines a weighted LS image-domain term with regularization based on sparsifying transforms learned from datasets of CT images. Numerical experiments with the NCAT phantom and clinical data show that the proposed method (DECT-ST) improves image quality and decomposition accuracy over direct matrix inversion decomposition and over PWLS decomposition with an edge-preserving hyperbola regularizer (DECT-EP).

2. PROBLEM FORMULATION

For image-domain DECT, we first use the sinograms at each energy to reconstruct a two-channel image vector $\mathbf{y} = (\mathbf{y}_H^T, \mathbf{y}_L^T)^T \in \mathbb{R}^{2N_p}$, where $\mathbf{y}_H, \mathbf{y}_L$ are the attenuation maps at high and low energy, respectively, and N_p is the number of pixels. Let $\mathbf{x} = (\mathbf{x}_1^T, \mathbf{x}_2^T)^T \in \mathbb{R}^{2N_p}$ denote the stacked unknown material density images, where $\mathbf{x}_l = (x_{l1}, x_{l2}, \dots, x_{ln}, \dots, x_{lN_p})^T \in \mathbb{R}^{N_p}$ denotes the l th material for $l = 1, 2$. We solve the following optimization problem to decompose $\mathbf{x} \in \mathbb{R}^{2N_p}$ from $\mathbf{y} \in \mathbb{R}^{2N_p}$ using two pre-learned ST matrices $\mathbf{\Omega}_1 \in \mathbb{R}^{m \times m}$ and $\mathbf{\Omega}_2 \in \mathbb{R}^{m \times m}$:

$$\min_{\mathbf{x} \in \mathbb{R}^{2N_p}} \frac{1}{2} \|\mathbf{y} - \mathbf{A}\mathbf{x}\|_{\mathbf{W}}^2 + \mathbf{R}(\mathbf{x}) \quad (1)$$

with the regularizer \mathbf{R} is defined as $\mathbf{R}(\mathbf{x}) \triangleq \min_{\{\mathbf{z}_{lj}\}} \sum_{l=1}^2 \sum_{j=1}^N \beta_l \left\{ \|\mathbf{\Omega}_l \mathbf{P}_{lj} \mathbf{x} - \mathbf{z}_{lj}\|_2^2 + \gamma_l^2 \|\mathbf{z}_{lj}\|_0 \right\}$, N is the number of image patches, operator $\mathbf{P}_{lj} \in \mathbb{R}^{m \times N_p}$ extracts the j th patch (overlapping patches assumed) of \mathbf{x}_l as a vector $\mathbf{P}_{lj} \mathbf{x}$, $\mathbf{z}_{lj} \in \mathbb{R}^m$ denotes the sparse coefficients for $\mathbf{P}_{lj} \mathbf{x}$, and the ℓ_0 “norm” counts the number of non-zeros in a vector. Parameters β_l for $l = 1, 2$, control the trade-off between noise and image

This work was supported in part by the SJTU-UM Collaborative Research Program, NSFC (61501292), Shanghai Pujiang Talent Program (15PJ1403900), NIH grant U01 EB018753, ONR grant N00014-15-1-2141, DARPA Young Faculty Award D14AP00086, and ARO MURI grants W911NF-11-1-0391 and 2015-05174-05. *Yong Long (email: yong.long@sjtu.edu.cn).

resolution and γ_l for $l = 1, 2$, control the sparsity in the model.

The $2N_p \times 2N_p$ mass attenuation coefficient matrix \mathbf{A} is defined as $\mathbf{A} = \mathbf{A}_0 \otimes \mathbf{I}_{N_p}$, where “ \otimes ” denotes the Kronecker product, and the 2×2 material decomposition matrix \mathbf{A}_0 is:

$$\mathbf{A}_0 = \begin{pmatrix} \varphi_{1H} & \varphi_{2H} \\ \varphi_{1L} & \varphi_{2L} \end{pmatrix}, \quad (2)$$

where φ_{lH} and φ_{lL} denote the mass attenuation coefficient of the l th material at high and low energy, respectively. In this work, these four values are obtained as $\varphi_{lH} = \mu_{lH}/\rho_l$ and $\varphi_{lL} = \mu_{lL}/\rho_l$ where ρ_l denotes the density of the l th material (1 g/cm³ for water and 1.92 g/cm³ for bone), and μ_{lH} and μ_{lL} denote the linear attenuation coefficient of the l th material at high and low effective energy, respectively. To obtain μ_{lH} and μ_{lL} , we manually select a uniform area in \mathbf{y}_H and \mathbf{y}_L (e.g., water region and bone region) respectively and compute the average pixel value in this area [2].

We assume that the acquired attenuation image \mathbf{y} is degraded by additive noise $\boldsymbol{\epsilon} \in \mathbb{R}^{2N_p}$ as $\mathbf{y} = \mathbf{A}\mathbf{x} + \boldsymbol{\epsilon}$. The statistical weight matrix \mathbf{W} in (1) is a $2N_p \times 2N_p$ diagonal matrix. Assuming that the low- and high-energy noise are uncorrelated [12] and the noise in each pixel of the attenuation images has equal variance [2], we rearrange the measurements and compose $\mathbf{W} = \mathbf{W}_j \otimes \mathbf{I}_{N_p}$ with N_p small (and identical) 2×2 diagonal matrices where $\mathbf{W}_j = \text{diag}(\sigma_H^2, \sigma_L^2)^{-1}$, and σ_H^2 and σ_L^2 denote the noise variances of the attenuation images at high and low energy, respectively. Each \mathbf{W}_j denotes the weighting matrix corresponding to the j th pixel. In this work, we compute \mathbf{W}_j by calculating the standard deviations of two uniform regions that are manually selected in the acquired attenuation images.

We compare the adaptive approach in (1) to DECT-EP [13], which differs from the proposed model in that the edge-preserving regularization is defined as $R(\mathbf{x}) = \sum_{l=1}^2 \beta_l R_l(\mathbf{x}_l)$, where the regularizer for the l th material is $R_l(\mathbf{x}_l) = \sum_{k=1}^K \psi_l([\mathbf{C}\mathbf{x}_l]_k)$, where $K = N_p N_{lp}$ with N_{lp} being the number of neighbors of pixel x_{lp} , $\mathbf{C} \in \mathbb{R}^{K \times N_p}$ is the finite difference matrix and $\psi_l(t) \triangleq \frac{\delta_l^2}{3} \left(\sqrt{1 + 3(t/\delta_l)^2} - 1 \right)$. The regularization term $R(\mathbf{x})$ here strengthens the smoothness of the decomposed material images while retaining boundary sharpness [2].

3. ALGORITHM

3.1. Sparsifying Transform (ST) Learning

We learn two sparsifying transforms Ω_1 and Ω_2 independently from patches extracted from a dataset of corresponding material images. The following transform learning problem is solved for $l = 1, 2$ using the algorithm in [10] that alternates between a ℓ_0 “norm” based sparse coding step (solving for \mathbf{Z}_l) and a non-convex transform update step (solving for Ω_l):

$$\min_{\Omega_l, \mathbf{Z}_l} \|\Omega_l \mathbf{Y}_l - \mathbf{Z}_l\|_F^2 + \lambda \left(\|\Omega_l\|_F^2 - \log |\det \Omega_l| \right) + \sum_{i=1}^{N'} \eta^2 \|\mathbf{Z}_{li}\| \quad (3)$$

where $\mathbf{Y}_1, \mathbf{Y}_2 \in \mathbb{R}^{m \times N'}$ are matrices of patches extracted from the two material images, N' is the number of training patches (for each material), $\lambda = \lambda_0 \|\mathbf{Y}_l\|_F^2$ where $\lambda > 0$ is a constant, η is a scalar parameter that controls the sparsity, $\mathbf{Z}_l \in \mathbb{R}^{m \times N'}$ for $l = 1, 2$, are matrices whose columns \mathbf{Z}_{li} are the sparse coefficients of the corresponding training patches in \mathbf{Y}_l . The term $\|\Omega_l \mathbf{Y}_l - \mathbf{Z}_l\|_F^2$ in (3) is called sparsification error, and denotes the deviation of the data in the transform domain from its sparse approximation. The term $\|\Omega_l\|_F^2 - \log |\det \Omega_l|$ is a regularizer preventing trivial solutions and controlling the transform condition number [10]. The cost of learning a ST in [10] scales as $O(m^2 I N')$ where m is the number of pixels in a patch and I is the number of iterations.

3.2. Optimization algorithm

We propose an algorithm for (1) that alternates between updating \mathbf{x} (*image update step*) and $\{\mathbf{z}_{lj}\}$ (*sparse coding step*) with other variables kept fixed.

3.2.1. Image update

With the sparse vectors \mathbf{z}_{lj} fixed, (1) reduces to the following penalized weighted least squares (PWLS) problem:

$$\min_{\mathbf{x} \in \mathbb{R}^{2N_p}} \frac{1}{2} \|\mathbf{y} - \mathbf{A}\mathbf{x}\|_{\mathbf{W}}^2 + \sum_{l=1}^2 \sum_{j=1}^N \beta_l \|\Omega_l \mathbf{P}_{lj} \mathbf{x} - \mathbf{z}_{lj}\|_2^2. \quad (4)$$

We solve (4) using FISTA-M [14, 15] (FISTA using a majorizer). For FISTA-M, the majorizer $\psi_M(\mathbf{x}; \mathbf{u})$ of $R_2(\mathbf{x})$, the second term in (4), is given by:

$$\psi_M(\mathbf{x}; \mathbf{u}) = R_2(\mathbf{u}) + \langle \nabla R_2(\mathbf{u}), \mathbf{x} - \mathbf{u} \rangle + \frac{1}{2} \|\mathbf{x} - \mathbf{u}\|_{\mathbf{M}}^2. \quad (5)$$

The matrix \mathbf{M} above is a diagonal majorizing matrix of $\nabla^2 R_2(\mathbf{x})$ defined as follows:

$$\mathbf{M} \succeq \nabla^2 R_2(\mathbf{x}) = 2 \sum_{l=1}^2 \beta_l \sum_{j=1}^N \mathbf{P}'_{lj} \Omega'_l \Omega_l \mathbf{P}_{lj}. \quad (6)$$

Ignoring constant terms in (5) yields the following update in FISTA-M:

$$\mathbf{x}^{(i+1)} = \arg \min_{\mathbf{x}} \frac{1}{2} \|\mathbf{y} - \mathbf{A}\mathbf{x}\|_{\mathbf{W}}^2 + \frac{1}{2} \|\mathbf{x} - \boldsymbol{\xi}^{(i)}\|_{\mathbf{M}}^2, \quad (7)$$

where $\boldsymbol{\xi}^{(i)} = \mathbf{u}^{(i)} - \mathbf{M}^{-1} \nabla R_2(\mathbf{u}^{(i)})$. We assume periodically positioned overlapping image patches with patch stride of 1 pixel, and that the patches beginning at image boundaries wrap around on the opposite side of the image. Then the entries of the diagonal matrix $\sum_{j=1}^N \mathbf{P}'_{lj} \mathbf{P}_{lj}$ corresponding to the l th material are equal to $m \mathbf{I}_{N_p}$ ($\mathbf{I}_{N_p} \in \mathbb{R}^{N_p \times N_p}$ is the identity matrix, while the entries corresponding to the other material are all zero. Therefore, the diagonal majorizer \mathbf{M} is: $\mathbf{M} = \text{diag}(2\beta_1 m \lambda_{\max}(\Omega'_1 \Omega_1), 2\beta_2 m \lambda_{\max}(\Omega'_2 \Omega_2)) \otimes \mathbf{I}_{N_p}$, where $\lambda_{\max}(\cdot)$ denotes the maximum eigenvalue of a matrix. Thus, we solve the image update problem in (4) by iterating over the following FISTA-M steps ($\forall j = 1, 2, \dots, N_p$) with $\theta^{(0)} = 1$ and $\mathbf{u}^{(0)} = \mathbf{x}^{(0)}$ being an appropriate initialization, and $\mathbf{B}_j = \mathbf{A}_0^T \mathbf{W}_j \mathbf{A}_0 + \mathbf{M}_j$ is precomputed for all j :

$$\begin{cases} \boldsymbol{\xi}^{(i)} = \mathbf{u}^{(i)} - \mathbf{M}^{-1} \nabla \mathbf{R}_2(\mathbf{u}^{(i)}) \\ \begin{pmatrix} x_{1j}^{(i+1)} \\ x_{2j}^{(i+1)} \end{pmatrix}^T = \mathbf{B}_j^{-1} (\mathbf{A}_0^T \mathbf{W}_j \mathbf{y}_j + \mathbf{M}_j \boldsymbol{\xi}_j^{(i)}) \\ \theta^{(i+1)} = \frac{1 + \sqrt{1 + 4\theta^{(i)^2}}}{2} \\ \mathbf{u}^{(i+1)} = \mathbf{x}^{(i+1)} + \frac{\theta^{(i)} - 1}{\theta^{(i+1)}} (\mathbf{x}^{(i+1)} - \mathbf{x}^{(i)}) \end{cases} \quad (8)$$

While (7) may appear computationally expensive because \mathbf{A} is large, we use the block diagonal structure in \mathbf{A} to separate the \mathbf{x} -update in (7) into N_p subproblems, i.e., the \mathbf{x} -update step in (8), where $\mathbf{M}_j \in \mathbb{R}^{2 \times 2}$ is a diagonal weighting matrix denoting the majorizing matrix for $(x_{1j}, x_{2j})^T$.

3.2.2. Sparse coding

With \mathbf{x} fixed, we update all \mathbf{z}_{lj} values by solving

$$\min_{\{\mathbf{z}_{lj}\}} \sum_{l=1}^2 \sum_{j=1}^N \beta_l \left\{ \|\boldsymbol{\Omega}_l \mathbf{P}_{lj} \mathbf{x} - \mathbf{z}_{lj}\|_2^2 + \gamma_l^2 \|\mathbf{z}_{lj}\|_0 \right\}. \quad (9)$$

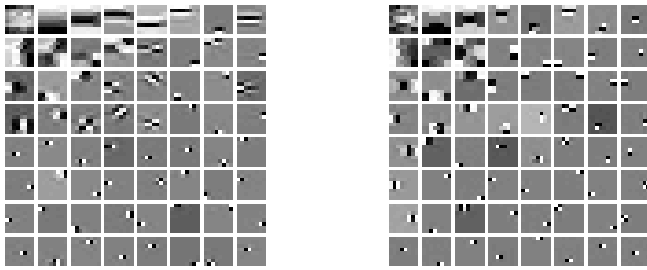
The solution is obtained by hard-thresholding as $\hat{\mathbf{z}}_{lj} = H_{\gamma_l}(\boldsymbol{\Omega}_l \mathbf{P}_{lj} \mathbf{x})$, $\forall l, j$. If the magnitude of b is no less than γ , the hard-thresholding operator (applied element-wise to a vector) $H_{\gamma}(b)$ returns b , else 0.

The cost of the proposed algorithm for I alternations scales as $O(m^2 I N_p)$ and is dominated by the matrix-vector products of the sparse coding step, since time-consuming forward and back-projections are not involved.

4. EXPERIMENTAL RESULTS

4.1. NCAT phantom study

We evaluate DECT-ST and compare its performance to those of the direct matrix inversion method and DECT-EP. We pre-learned two ST matrices from five slices of water and bone images of the XCAT phantom [16] (different from test image) using (3), respectively. We extracted image patches of size 8×8 . For water and bone, we chose λ and η as $\{5.28 \times 10^8, 0.12\}$ and $\{9.74 \times 10^7, 0.15\}$, respectively. We ran 2000 iterations of the transform learning algorithm [10] to ensure convergence. Fig. 1 shows the learned ST matrices with each row displayed as an 8×8 patch.



(a) transform for water (b) transform for bone
Fig. 1: Rows of learned transforms shown as 8×8 patches.

The simulated true NCAT images were 1024×1024 and the pixel size was $0.49 \times 0.49 \text{ mm}^2$. We generated sinograms of size 888×984 using GE LightSpeed X-ray CT fan-beam system geometry corresponding to a poly-energetic source at 80kVp and 140kVp with 1.86×10^5 and 1×10^6 incident

photons per ray, respectively. A total of 984 projections over 360° were obtained for each CT scan. We used filtered back projection (FBP) to reconstruct 2D high and low energy attenuation images of size 512×512 , where the pixel size was $0.98 \times 0.98 \text{ mm}^2$.

We calculated the basis material images from attenuation images via matrix inversion to initialize the DECT-EP method. The DECT-EP method converges quickly in image domain. For the proposed method, we used the images obtained with the DECT-EP method as the initialization. For DECT-EP, β_l was set as $2^{8.5}$ and 2^9 for water and bone respectively, and $\delta_1 = 0.01 \text{ g/cm}^3$ and $\delta_2 = 0.02 \text{ g/cm}^3$. For DECT-ST, the parameters β_1, β_2 , and γ_1, γ_2 , were set as $\{25, 27, 0.06, 0.05\}$. We empirically selected optimal parameter combinations for DECT-ST and DECT-EP to achieve the best image quality and decomposition accuracy.

To evaluate performance, we computed the Root Mean Square Error (RMSE) for the decomposed material images. For a decomposed material image $\hat{\mathbf{x}}_l$, RMSE is defined as $\sqrt{\frac{1}{N_p} \sum_{j=1}^{N_p} (\hat{x}_{lj} - x_{lj}^*)^2}$, where x_{lj}^* denotes the down-sampled true density of the l th material at the j th pixel location. Table 1 summarizes the RMSE of three different methods. The proposed method further decreases the RMSE achieved by DECT-EP or with direct matrix inversion.

Method	Direct Inversion	DECT-EP	DECT-ST
Water	77.7	40.2	35.0
Bone	78.7	53.7	46.2

Table 1: RMSE of decomposed images of basis materials by different methods. The unit of RMSE is 10^{-3} g/cm^3 .

Fig. 2 shows zoom-ins of specific regions in the water and bone decompositions. The proposed method successfully differentiates basis materials and suppresses the high noise in the direct matrix inversion method. In addition, the proposed method provides better edges compared to DECT-EP.

4.2. Patient study

The patient data were obtained by Siemens SOMATOM Force CT scanner using dual-energy CT imaging protocols. The CT scanner applied the dual-source at 80kVp and 150kVp for dual-energy data acquisition. The CT images of the patient's thigh are shown in Fig. 3.

We used the same learned transforms (from XCAT) as in Section 4.1. We used basis images calculated from matrix inversion as initialization for the DECT-EP method and the DECT-EP result was used as initialization for DECT-ST. For DECT-EP, (β, δ) were set as $\{2^{11}, 0.008\}$ and $\{2^{12}, 0.015\}$ for water and bone, respectively. For DECT-ST, the parameters (β_1, β_2) and (γ_1, γ_2) were set as $\{2 \times 10^2, 3 \times 10^2\}$ and $\{0.012, 0.024\}$. Results in Fig. 4 show that the proposed DECT-ST provides better image edges, improved decomposition accuracy and decreased cross-talk compared to the other two methods.



Fig. 2: First to fourth row: material images of ground truth, direct matrix inversion decomposition, DECT-EP, and the proposed DECT-ST, respectively. Water images are in the first column with display window $[0.25\ 1.6]\ \text{g/cm}^3$, and bone images are in the second column with narrower window $[0.12\ 0.25]\ \text{g/cm}^3$, to highlight differences in decomposed basis material images.

5. CONCLUSIONS

We proposed a new method for DECT that combines an image-domain WLS term with regularizer involving learned sparsifying transforms, and demonstrated that the proposed DECT-ST method outperformed the DECT-EP method (which uses a fixed finite differencing type sparsifying model) in terms of image quality and material decomposition accuracy for both simulated and clinical studies. In future work, we

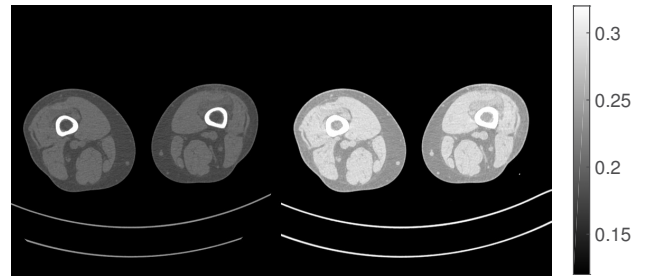


Fig. 3: Thigh CT images of a patient. Left image is at the high-energy: 150 kVp, and the right image is at the low-energy: 80 kVp. Display window is $[0.12\ 0.32]\ \text{cm}^{-1}$.

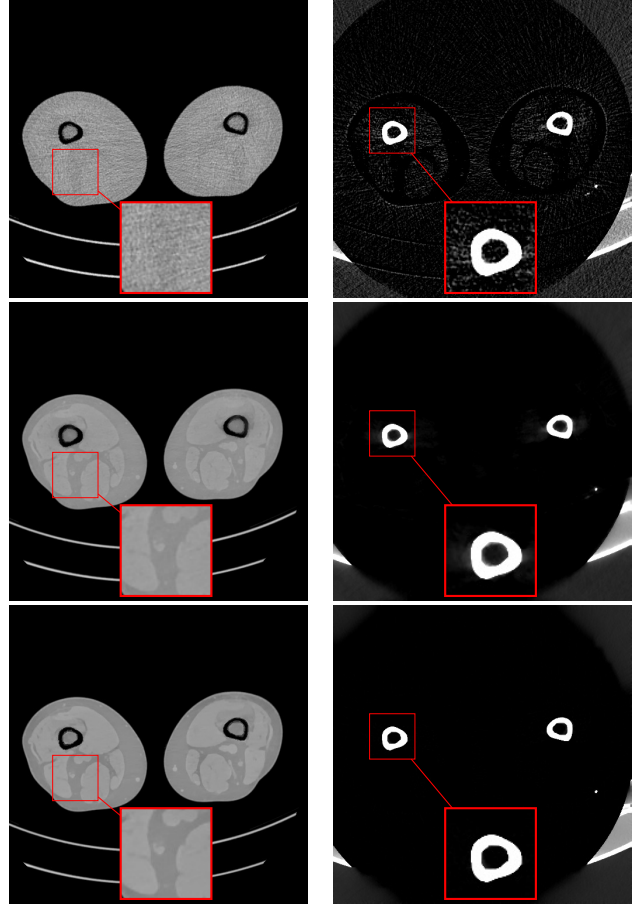


Fig. 4: First to third row: material images of direct matrix inversion decomposition, DECT-EP, and the proposed DECT-ST, respectively. Water and bone images are in the first (display window $[0.25\ 1.5]\ \text{g/cm}^3$) and second (display window $[0\ 0.3]\ \text{g/cm}^3$) columns, respectively.

will investigate cross-material ST that accounts for correlation between material images, for example, material images share common edges. We will investigate reconstruction methods using a more accurate DECT measurement model [5] with ST-based regularization.

6. ACKNOWLEDGEMENT

The authors thank Dr. Tianye Niu, Zhejiang University, for providing clinical DECT images for our experiments.

7. REFERENCES

- [1] P. R. Mendonca, P. Lamb, and D. V. Sahani, "A flexible method for multi-material decomposition of dual-energy CT images," *IEEE Trans. Med. Imag.*, vol. 33, no. 1, pp. 99–116, 2014.
- [2] T. Niu, X. Dong, M. Petrongolo, and L. Zhu, "Iterative image-domain decomposition for dual-energy CT," *Med. Phys.*, vol. 41, no. 4, pp. 041901, Apr. 2014.
- [3] J. Harms, T. Wang, M. Petrongolo, T. Niu, and L. Zhu, "Noise suppression for dual-energy ct via penalized weighted least-square optimization with similarity-based regularization," *Med. Phys.*, vol. 43, no. 5, pp. 2676–86, 2016.
- [4] J. Noh, J. A. Fessler, and P. E. Kinahan, "Statistical sinogram restoration in dual-energy CT for PET attenuation correction," *IEEE Trans. Med. Imag.*, vol. 28, no. 11, pp. 1688–702, Nov. 2009.
- [5] Y. Long and J. A. Fessler, "Multi-material decomposition using statistical image reconstruction for spectral CT," *IEEE Trans. Med. Imag.*, vol. 33, no. 8, pp. 1614–26, Aug. 2014.
- [6] Q. Xu, H. Yu, X. Mou, L. Zhang, J. Hsieh, and G. Wang, "Low-dose X-ray CT reconstruction via dictionary learning," *IEEE Trans. Med. Imag.*, vol. 31, no. 9, pp. 1682–97, Sept. 2012.
- [7] K. Mechlem, S. Allner, K. Mei, F. Pfeiffer, and P. B. Noël, "Dictionary-based image denoising for dual energy computed tomography," in *Proc. SPIE 9783 Medical Imaging 2016: Phys. Med. Im.*, 2016, pp. 97830E–1–97830E–7.
- [8] Y. Zhang, X. Mou, H. Yu, G. Wang, and Q. Xu, "Tensor based dictionary learning for spectral CT reconstruction," *IEEE Trans. Med. Imag.*, vol. 36, no. 1, pp. 142–54, 2017.
- [9] L. Li, Z. Chen, and P. Jiao, "Dual-energy CT reconstruction based on dictionary learning and total variation constraint," in *Proc. IEEE Intl. Symp. Biomed. Imag.*, 2012, pp. 2358–61.
- [10] S. Ravishankar and Y. Bresler, " l_0 sparsifying transform learning with efficient optimal updates and convergence guarantees," *IEEE Trans. Sig. Proc.*, vol. 63, no. 9, pp. 2389–404, May 2015.
- [11] X. Zheng, Z. Lu, S. Ravishankar, Y. Long, and J. A. Fessler, "Low dose CT image reconstruction with learned sparsifying transform," in *Proc. IEEE Wkshp. on Image, Video, Multidim. Signal Proc.*, July 2016, pp. 1–5.
- [12] R. Zhang, J. B. Thibault, C. A. Bouman, K. D. Sauer, and J. Hsieh, "Model-based iterative reconstruction for dual-energy X-ray CT using a joint quadratic likelihood model," *IEEE Trans. Med. Imag.*, vol. 33, no. 1, pp. 117–34, Jan. 2014.
- [13] Y. Xue, R. Ruan, X. Hu, Y. Kuang, J. Wang, Y. Long, and T. Niu, "Statistical image-domain multi-material decomposition for dual-energy CT," *Med. Phys.*, vol. 44, no. 3, pp. 886–901, 2017.
- [14] S. Ravishankar and Y. Bresler, "Doubly sparse transform learning with convergence guarantees," in *Proc. IEEE Conf. Acoust. Speech Sig. Proc.*, 2014, pp. 5262–6.
- [15] M. J. Muckley, D. C. Noll, and J. A. Fessler, "Fast parallel MR image reconstruction via B1-based, adaptive restart, iterative soft thresholding algorithms (BARISTA)," *IEEE Trans. Med. Imag.*, vol. 34, no. 2, pp. 578–88, 2015.
- [16] W. P. Segars, M. Mahesh, T. J. Beck, E. C. Frey, and B. M. W. Tsui, "Realistic CT simulation using the 4D XCAT phantom," *Med. Phys.*, vol. 35, no. 8, pp. 3800–8, 2008.